Synthesis, Characterization, and Photocatalytic Application of α-Fe_2O_3/α-$AgVO_3$ Nanocomposite for Removal of Methylene Blue from Aqueous Media

Shariatzadeh, Seyed Mohammad Reza; Salimi, Mahmoud*+

Department of Chemical Engineering, Arak Branch, Islamic Azad University, Arak, I.R. IRAN

Fathinejad, Hasan

Department of Chemistry, Farahan Branch, Islamic Azad University, Farahan, I.R. IRAN

Hassani Joshaghani, Ali

Department of Chemical Engineering, Arak Branch, Islamic Azad University, Arak, I.R. IRAN

ABSTRACT: *In this study, α-Fe_2O_3/α-$AgVO_3$ nanocomposite was successfully synthesized via a solvothermal process, followed by a co-precipitation method. The products were characterized by X-Ray Diffraction (XRD), Field Emission Scanning Electron Microscopy (FESEM), Energy Dispersive X-ray (EDX) spectroscopy, Fourier Transform InfraRed (FT-IR) spectroscopy, Diffuse Reflectance Spectroscopy (DRS). The photocatalytic activity of α-Fe_2O_3/α-$AgVO_3$ nanocomposite was investigated for the removal of Methylene Blue (MB) dye from aqueous solutions under UltraViolet (UV) light irradiation. The results revealed that the photocatalytic performance of the nanocomposite is higher than that of the pure compounds. The effect of pH, MB concentration, and photocatalyst dosage on the removal efficiency of MB was also evaluated. The solution pH of 5.9, MB concentration of 20 mg/L, and photocatalyst dosage of 1.5 g/L were obtained as the optimal conditions. The kinetics of MB degradation was studied, and it was found that the reaction follows the pseudo-first-order equation. Under the optimal conditions, the MB removal efficiency of 98% was obtained, and the rate constant was calculated to be 0.0312 min^{-1}. A possible mechanism for the p-n heterojunction was proposed to describe the enhanced photocatalytic activity of the α-Fe_2O_3/α-$AgVO_3$ nanocomposite. The findings demonstrated that the α-Fe_2O_3/α-$AgVO_3$ nanocomposite with improved photocatalytic activity can be used to remove contaminants from aqueous media.*

KEYWORDS: *α-Fe_2O_3 (Hematite); Nanocomposite; Solvothermal process; Photocatalytic activity; p-n heterojunction.*

INTRODUCTION

In recent decades, chemical pollution has adversely affected the environment and human health. The elimination of chemical pollutants is crucial, as they can persist in the environment and

* *To whom correspondence should be addressed.*
+E-mail address: s.khan@gu.edu.pk; shafi.ics.gu@gmail.com
1021-9986/2023/4/1192-1203 12/$/6.02

cause damaging effects [1, 2]. Organic dyes are a significant source of water contamination and are classified as environmentally hazardous. These chemicals are widely utilized in different industries, including textiles, paper, printing, food, and cosmetics. For example, cationic dyes like methylene blue ($C_{16}H_{18}N_3SCl$) are essential chemical molecules with various industrial applications suspected of posing health and environmental risks. Many of these chemicals cause human health issues such as skin diseases, cancer, and mutation. Thus, removing contaminants such as dyes from water is of essential importance [3, 4]. Many techniques, including advanced oxidation processes (AOPs), have been utilized to remove organic contaminants from aqueous media. Among AOPs, heterogeneous photocatalysis has received considerable interest as a cost-effective and environmentally benign technique [5, 6]. Various semiconductor metal oxides such as TiO_2 [7], α-Fe_2O_3 [1], CuO [8], ZnO [9], MgO [10], and hybrid of metal oxides [11] have been used in the photocatalysis process. However, some weak points such as wide band gap, low conductivity, and high recombination rate of charge carriers have restricted the photocatalytic applications of semiconductors. Hence, many attempts have been devoted to overcoming these restrictions. The main modifications for improving the photocatalytic activity of semiconductors include (1) doping with metal or non-metal elements [12], (2) heterojunction with other semiconductors, and (3) surface plasmonic resonance by deposition of a noble metal on the surface of particles [13].

α-Fe_2O_3 (hematite) is an n-type semiconductor that has been widely studied for photocatalytic applications due to its unique properties such as stability, low cost, narrow band gap, abundance, and non-toxicity [14]. α-Fe_2O_3 nanostructures can be synthesized via different methods, including hydrolysis, co-precipitation, hydrothermal method, solvothermal method, thermal dehydration, sol-gel, and solid-state reaction [15]. The hydrothermal and solvothermal methods are one-step processes with the possibility of controlling particle size and morphology and have been widely used to synthesize different shapes of α-Fe_2O_3 [16]. Different morphologies of α-Fe_2O_3, including nanoplatelets [17], hexagonal plates [18], rod and ellipsoidal [19], flowerlike [20], and 3D multileaf [21], have been successfully prepared using the hydrothermal or solvothermal treatment. Despite the advantages of hematite, some weaknesses, such as low conductivity and high recombination rate of charge carriers, restrict its application as a photocatalyst [22]. As a modification method, the heterojunction between α-Fe_2O_3 and other semiconductors can improve the photocatalytic performance of α-Fe_2O_3 [23].

$AgVO_3$ is a p-type semiconductor with remarkable photocatalytic activity [24]. $AgVO_3$ nanostructures with various morphologies such as nanorods [25], nanowires [26], nanobelts [27], and nanoribbons [28] have been prepared via hydrothermal and co-precipitation routes. To the best of our knowledge, no research has been conducted on the synthesis and photocatalytic activity of a hybrid of α-Fe_2O_3 and α-$AgVO_3$. This research aimed to synthesize novel α-Fe_2O_3/α-$AgVO_3$ nanocomposite and investigate the photocatalytic activity of the material. In a slurry annular photoreactor, the photocatalytic performance of the nanocomposite was compared with the pure components by measuring the degradation of MB as a pollutant model under UV light irradiation. The effect of reaction parameters including pH, MB concentration, and photocatalyst dosage on the removal efficiency of MB was studied. The kinetics of photocatalytic degradation of MB was also investigated.

EXPERIMENTAL SECTION

Materials

Ferric chloride hexahydrate (99.5% $FeCl_3.6H_2O$, Merck), urea (99.5%, ChemLab), and anhydrous ethanol (99.9% C_2H_5OH, Merck) were used to synthesize α-Fe_2O_3 nanostructures. Ammonium

metavanadate (NH_4VO_3, Merck) and silver nitrate ($AgNO_3$, Sigma) were used to synthesize α-$AgVO_3$. Deionized water was used in all cases. All the materials were of analytical grade and used without further purification.

Synthesis of catalysts

Synthesis of α-Fe_2O_3

α-Fe_2O_3 was prepared *via* a solvothermal process according to the previous work [29]. In a typical synthesis, 1.323 g of $FeCl_3.6H_2O$ and 0.441 g of urea were dissolved in 70 mL of ethanol. The mixture was magnetically stirred at room temperature for 30 min to obtain a clear and homogeneous solution. The obtained solution was transferred into a 100 mL teflon-lined stainless steel autoclave, sealed, and heated in an oven at 180 °C for 8 h. Then, the autoclave was naturally cooled down to room temperature. The precipitates were collected by centrifugation, washed with ethanol several times, and dried in an oven at 80 °C for 4 h.

Synthesis of α-$AgVO_3$

α-$AgVO_3$ was synthesized by a co-precipitation method [30]. In a typical synthesis, 0.117 g of NH_4VO_3 was dissolved in 80 mL of distilled water and magnetically stirred. Then 0.170 g of $AgNO_3$ was dissolved in 40 mL of distilled water. Afterward, the $AgNO_3$ solution was added to the NH_4VO_3 solution drop by drop, and the reaction was continued for 3 hours in the temperature range of 35-40 °C in the dark. Finally, the precipitates were collected by centrifugation, washed with water and ethanol in turn, and dried in an oven at 80 °C for 5 h.

Synthesis of α-Fe_2O_3/α-$AgVO_3$ nanocomposite

For the synthesis of α-Fe_2O_3/α-$AgVO_3$ (FAV) nanocomposite, 0.200 g of the as-prepared α-Fe_2O_3 powder was ultrasonically dispersed in 40 mL of distilled water. A 0.120 g of NH_4VO_3 was dissolved in 40 mL of distilled water until a yellow solution was obtained. A 0.170 g $AgNO_3$ was dissolved in 20 mL of distilled water. The NH_4VO_3 solution was added dropwise to the hematite suspension under vigorous stirring. Then, $AgNO_3$ solution was added dropwise to the α-Fe_2O_3-NH_4VO_3 suspension under stirring, and the reaction was continued for 3 hours in the temperature range of 35-40 °C until light brown precipitates were obtained. The precipitates were separated by centrifugation, washed with ethanol and distilled water several times, and dried at 80 °C for 5 h.

Characterization

The crystal structure of products was determined by XRD on XRD PANanalytical with Cu Kα radiation at λ=1.54060 Å. The morphology of samples was investigated by FESEM with MIRA3TESCAN-XMU. The chemical composition of samples was determined by EDX along with FESEM. The type of bonding structure was examined by FT-IR with Thermo AVATAR. The optical property of samples was determined by DRS with Avantes-Avaspec-2048.

Photocatalytic experiments

The photocatalytic activity of the as-prepared nanocomposite was evaluated by the photodegradation of methylene blue dye as a model pollutant under UV light irradiation. For photocatalytic experiments, a lab-scale slurry annular photoreactor was built (Fig. 1). A 250-mL cylindrical tube with a working volume of 100 mL was used as the reaction vessel. A UV lamp (6 W, Philips, irradiation intensity = 3.8 mW/cm^2) with the main emission at 254 nm was located inside the vessel, and a quartz tube was used to separate the UV lamp from the reaction suspension. A cooling water jacket provided water with a continuous flow to keep the reaction temperature in the range of 25-27 °C. An air pump supplied the oxygen needed for the photo-oxidative reaction. For each photocatalytic experiment, a specific amount of the photocatalyst powder was ultrasonically dispersed in 100 mL of MB dye solution. Before irradiation, the reaction suspension was magnetically stirred in the dark for 90 minutes

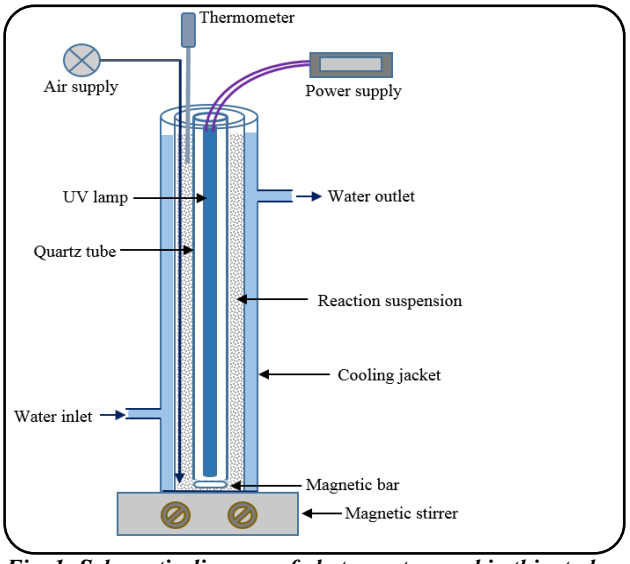

Fig. 1: Schematic diagram of photoreactor used in this study.

to attain the adsorption-desorption equilibrium point between MB and the photocatalyst. Then, the suspension was exposed to UV light illumination under mixing and aerating. In regular intervals of 30 min, the suspension samples were taken, centrifuged, and the concentration of MB was measured at 664 nm by a Hach 2800 Vis spectrophotometer. The following equation was used to calculate the removal efficiency of MB:

$$\eta(\%) = \frac{C_0 - C}{C_0} \times 100 \quad (1)$$

Where η is the removal efficiency, and C_0 and C are the initial concentration of MB and the concentration of MB at a specific time, respectively.

Kinetics study

The Langmuir-Hinshelwood model was used to study the kinetics of MB photodegradation [31]. According to this model, the kinetics of the reaction can be explained by the following pseudo-first-order equation:

$$\ln (C_0/C) = kt + s \quad (2)$$

Where k is the rate constant (min^{-1}), t is the irradiation time (min), and s is a constant parameter that shows the adsorption capacity of the photocatalyst.

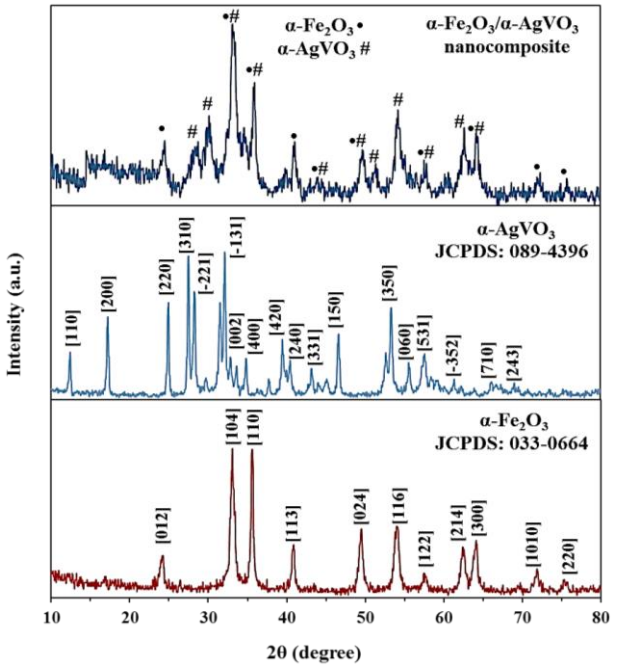

Fig. 2: XRD pattern of the α-Fe2O3, α-AgVO3, and FAV nanocomposite.

RESULTS AND DISCUSSION

Characterization

The crystal structure of the products was determined by XRD analysis. The XRD patterns of the pure α-Fe_2O_3, pure α-$AgVO_3$, and α-Fe_2O_3/α-$AgVO_3$ nanocomposite are shown in Fig. 2. The XRD pattern for the pure α-Fe_2O_3 sample illustrates diffraction peaks that can be well ascribed to the standard peaks of the hematite structure with JCPDS 033-0664 [32]. This pattern shows no peaks related to impurities and confirms that the α-Fe_2O_3 has been successfully synthesized via the solvothermal method. In the XRD pattern of the α-$AgVO_3$ sample, all diffraction peaks can be well indexed to the standard peaks of the α-$AgVO_3$ with JCPDS 089-4396 [33]. In the XRD pattern of FAV nanocomposite, the characteristic and overlapping peaks of the α-Fe_2O_3 and α-$AgVO_3$ can be observed, which confirms the presence of the pure compounds in FAV nanocomposite.

The morphology of the products was characterized using the FESEM. Fig. 3 shows the FESEM images of the α-Fe_2O_3, α-$AgVO_3$, and FAV at different magnifications. As can be seen in Fig. 3(a), the pure

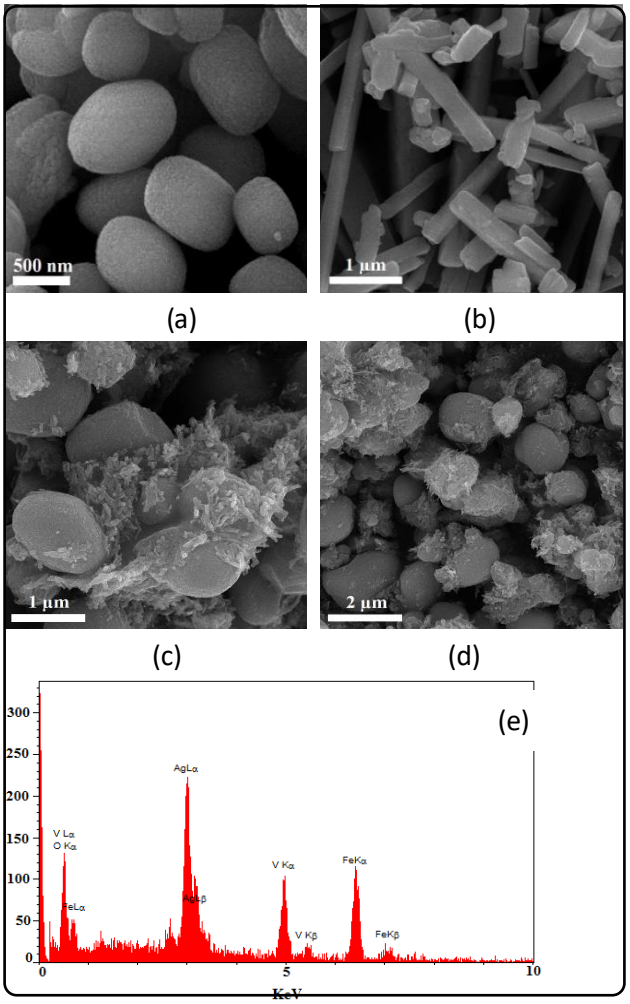

Fig. 3: FESEM Images of the A-Fe2O3 (A), A-Agvo3 (B), FAV Nanocomposite (C,D), and EDX Pattern Of The FAV Nanocomposite (E).

α-Fe_2O_3 consists of distorted microspheres with an average diameter size of around 1 µm. The microspheres are composed of nanoparticles with diameters in the range of 10 to 30 nm. Hematite nanostructures with similar morphologies were prepared in previous studies. *Tadic et al*. synthesized ellipsoid-like 3D hematite superstructures with diameters around 1.5 µm composed of self-assembled nanoparticles with sizes around 50 nm by a hydrothermal process [34]. *Trpkov et al*. obtained hematite microparticles with dimensions of 2.7 µm with nanoparticle sub-units using a hydrothermal route [35]. In another research, iron oxide nanocomposite was prepared with the morphology of nanoclusters covered with silica

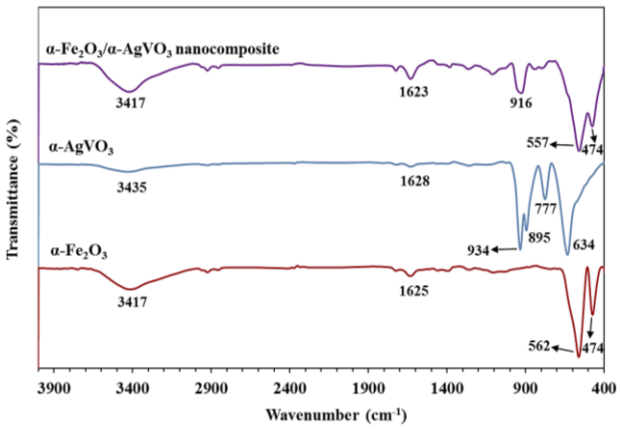

Fig. 4: FT-IR spectra of α-Fe2O3, α-AgVO3, and FAV nanocomposite.

with diameters of about 100 nm and their hierarchical assemblies with a bundle-like morphology of 8 µm-length and 1µm-width [36]. The FESEM image in Fig. 3(b) shows the morphology of microrods for the pure α-$AgVO_3$. Fig. 3(c) and 3(d) show the FESEM image of the FAV nanocomposite in different magnifications and evince that α-$AgVO_3$ microrods have been attached to the surface of the nanostructured α-Fe_2O_3 microspheres. The EDX pattern was taken to specify the composition of the samples. As shown in Fig. 3(d), the EDX pattern shows the elements Fe, O, Ag, and V in the structure of FAV nanocomposite.

The chemical structure of the products was studied by FT-IR analysis. The FT-IR spectra were obtained in the wavenumber range from 400 to 4000 cm^{-1} at room temperature. As shown in Fig. 4, in the pure α-Fe_2O_3 spectrum, two vibrational bands at 474 and 562 cm^{-1} related to the Fe-O stretching modes confirm the formation of α-Fe_2O_3 crystals. The bands at 1625 and 3417 cm^{-1} are related to the bending and stretching modes of the O-H groups, respectively, which show the presence of the hydroxyl group and/or water molecules on the surface of α-Fe_2O_3 [37]. In the spectrum of the pure $AgVO_3$, the absorption bands at 634, 777, 895, and 934 cm^{-1} are related to the symmetric and asymmetric stretching vibrations of VO_3. The absorption bands at 1628 and 3435 cm^{-1} are attributed to the vibrational modes of the hydroxyl group on the surface of the $AgVO_3$ [38]. The spectrum of as-synthesized nanocomposite

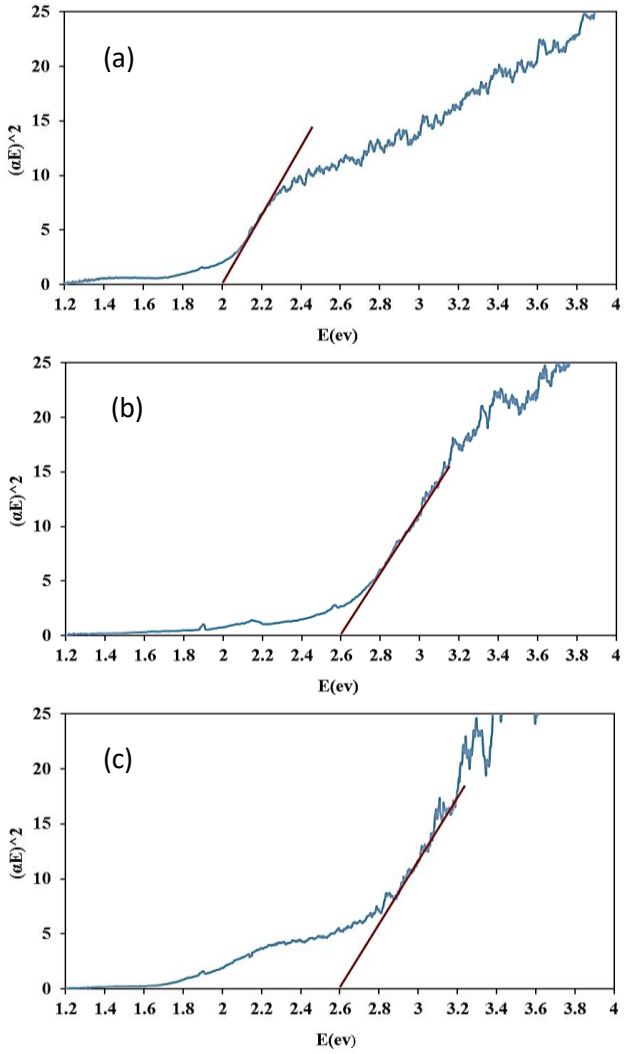

Fig. 5: UV-Vis spectra and band gap of pure α-Fe_2O_3 (a), pure α-$AgVO_3$ (b), and FAV nanocomposite (c).

shows overlapping of the absorption peaks of α-Fe_2O_3 and α-$AgVO_3$, which indicates the presence of these pure compounds in the composition of FAV nanocomposite.

The UV-Vis spectra of the pure compounds and the nanocomposite is shown in Fig. 5(a-c). The optical band gap (E_g) was determined by the Kubelka-Munk equation using UV-vis DRS. The band gap was calculated by plotting $(\alpha h\nu)^2$ vs $h\nu$ and extrapolating the linear component of UV-Vis absorbance curve. For the pure α-Fe_2O_3 and α-$AgVO_3$, Eg was determined to be 2.0 and 2.6, respectively, which are compatible with reported

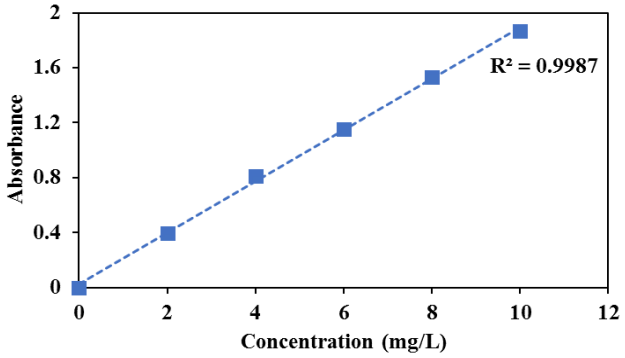

Fig. 6: The calibration curve obtained for MB at 664 nm.

values in the literature [15, 38]. For FAV nanocomposite the band gap was obtained to be 2.6, showing the energy is mainly absorbed by α-$AgVO_3$.

Photocatalytic degradation of MB

A calibration curve for MB was provided by a spectrophotometer at 664 nm. MB solutions with a concentration of 0 to 10 mg/L were used to obtain the calibration curve. As shown in Fig. 6, the absorbance is linearly dependent on MB concentration with R^2 = 0.9987. This calibration curve was used for measuring MB concentration in photocatalytic experiments. To measure the MB concentrations higher than 10 mg/L, the solutions were diluted to the concentration within the calibration curve range.

The photocatalytic activity of the as-prepared photocatalysts was evaluated by the photocatalytic degradation of MB dye under UV light irradiation. The photocatalytic experiments were performed at inherent pH of MB solution of 5.9, an initial MB concentration of 20 mg/L, and a photocatalyst dosage of 1.0 g/L. The plots of C/C_0 versus time are depicted in Fig. 7. For the blank solution without photocatalyst, MB concentration slightly decreased, which shows the photostability of MB dye under UV light irradiation. The as-prepared photocatalysts showed different capacities for the adsorption of MB during the dark stage. The adsorptive removal efficiency of MB for α-Fe_2O_3, α-$AgVO_3$, and FAV nanocomposite was 2%, 29%, and 36%, respectively.

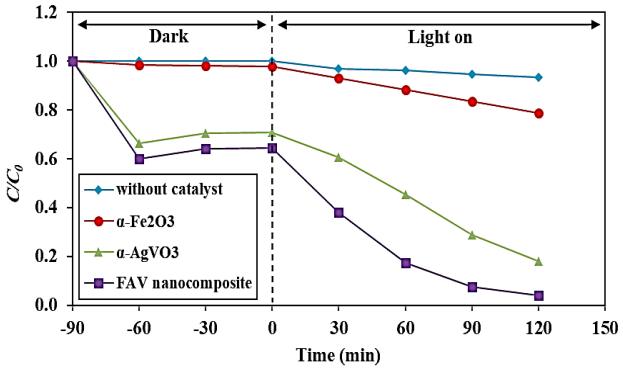

Fig. 7: Plots of photodegradation rate of MB under UV light illumination for the photocatalysts (initial MB solution pH=5.9, initial MB concentration=20 mg/L, photocatalyst dosage=1.0 g/L).

Thus, the FAV nanocomposite shows a higher adsorption capacity favored for photocatalytic degradation. During light irradiation, MB concentration decreased, and after 120 min of irradiation, the removal efficiency of MB was obtained at 21%, 82%, and 96% for α-Fe_2O_3, α-$AgVO_3$, and FAV nanocomposite, respectively. Compared with the pure α-Fe_2O_3 and pure α-$AgVO_3$, the FAV nanocomposite showed a superior removal efficiency of MB. The enhanced removal efficiency is attributed to the synergistic effect of adsorption and photocatalytic activity of the FAV nanocomposite. Higher adsorption capacity provides more active sites accessible to the dye species and promotes the decomposition rate of MB. In addition, the heterojunction between the α-Fe_2O_3 and α-$AgVO_3$ in FAV nanocomposite improves the separation of electrons and holes, leading to a lower recombination rate of charge carriers. This increases the number of photogenerated electrons and holes and facilitates the degradation of MB dye [39].

Effect of reaction parameters on the MB degradation

The effect of photocatalytic reaction parameters, including pH, MB concentration, and FAV nanocomposite dosage, on the degradation of MB was investigated. Fig. 8(a) shows the degradation rate of MB in pH of 5.9, 8.0, 9.2, and 11.1 at MB concentration of 20 mg/L and FAV dosage of 1.0 g/L. As can be seen, pH has a negligible effect on the

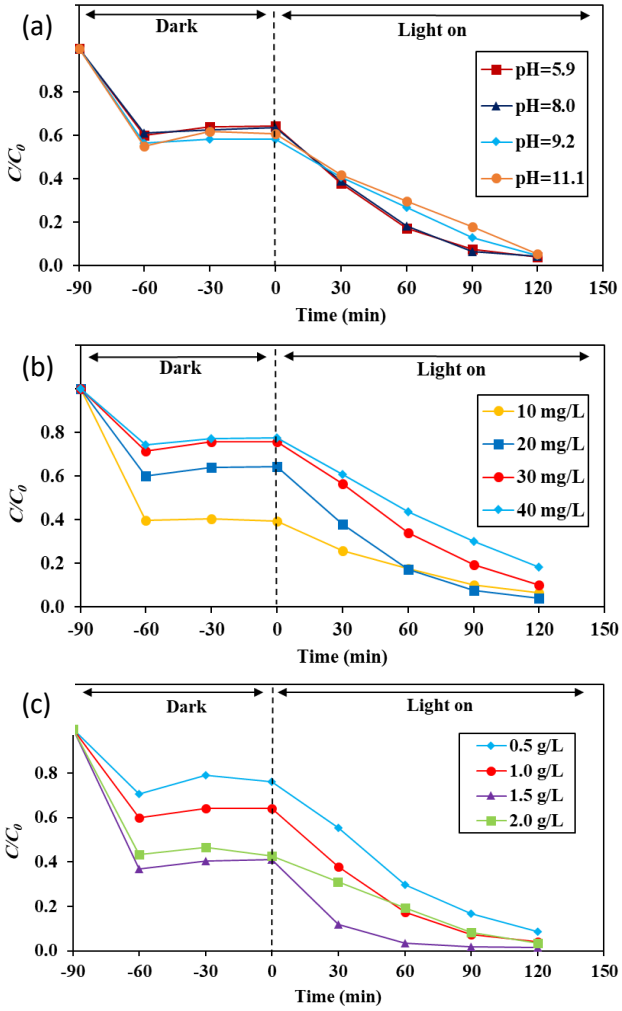

Fig. 8: Effect of pH (a), MB concentration (b), and FAV dosage (c), on the MB removal.

degradation rate of MB, and the removal efficiency was obtained at 96% in all experiments. The constant removal efficiency shows that increasing pH does not affect the interaction between MB species and the surface of photocatalyst particles. This is attributed to the adsorption of MB dye into the gel texture of α-$AgVO_3$, which predominates the interactions between cationic MB dye and anionic hydroxyl groups on the surface of nanocomposite [40]. Thus, the adsorption capacity and photocatalytic activity of the nanocomposite remain almost unchanged. Accordingly, the subsequent experiments were accomplished at the inherent pH of MB solutions (pH=5.9).

Fig. 8(b) shows the photocatalytic degradation rate for different MB concentrations at FAV dosage of 1.0 g/L. For MB concentrations of 10, 20, 30, and 40 mg/L, the removal efficiency of 94, 96, 90, and 82% was obtained, respectively. The maximum removal efficiency was obtained for MB concentration of 20 mg/L. With increasing MB concentration from 10 to 20 mg/L, more MB species are accessible in the photocatalytic reaction. When MB concentration increases to 30 and 40 mg/L, less portion of the MB can reach the surface of the photocatalyst particles, and fewer active sites are accessible to the MB species, which leads to a decrease in the photocatalytic degradation rate and removal efficiency of MB [41].

Fig. 8(c) shows the photocatalytic degradation rate for different dosages of FAV nanocomposite at MB concentration of 20 mg/L. The removal efficiency for nanocomposite dosage of 0.5, 1.0, 1.5, and 2.0 g/L was 91%, 96%, 98%, and 96%, respectively. With increasing the photocatalyst dosage from 0.5 to 1.5 g/L, adsorption capacity and active sites of the photocatalyst increases accordingly. Thus, more photogenerated electrons and holes are provided for the oxidative degradation of MB species, which leads to the enhancement of the photodegradation rate and removal efficiency of MB. More increase in the photocatalyst dosage to 2.0 g/L increases the turbidity of the suspension and decreases the intensity of light, leading to a decrease in the photodegradation efficiency [42].

Kinetics of MB photodegradation

The plots of ln (C_0/C) versus irradiation time are shown in Fig. 9(a-c). Data fitting and calculated correlation coefficients for the linear plots using equation (2) confirm that the photocatalytic degradation of MB over FAV nanocomposite follows the pseudo-first-order kinetics [43, 44]. The pseudo-first-order rate constants for different conditions are shown in Tables 1 to 3. The maximum rate constant of 0.0312 min^{-1} was obtained under the optimal conditions.

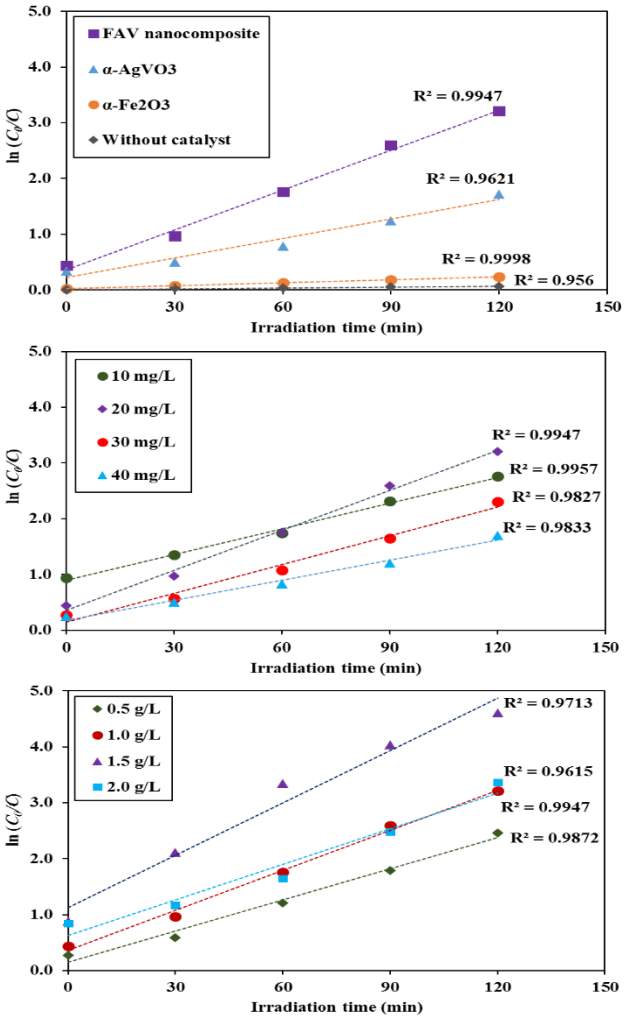

Fig. 9: Kinetic plots of the photodegradation of MB, for the photocatalysts (a), for different initial MB concentrations (b), and for different FAV dosages (c).

The removal efficiencies of MB by adsorption and photodegradation are shown in Tables 1 to 3. According to data in Table 2, for lower concentrations, adsorption is the predominant process, and photodegradation has less contribution to MB removal. Based on data in Table 3, for higher catalyst dosages, adsorption is the predominant process, and the contribution of photodegradation in the MB removal decreases. The optimal conditions were obtained at the inherent pH of MB solution of 5.9, initial MB concentration of 20 mg/L, and catalyst dosage of 1.5 g/L. Under these conditions, the final

Table 1: The Removal efficiency of MB and rate constant by the as-prepared photocatalysts.

Photocatalyst	Removal efficiency (adsorption)	Removal efficiency (photodegradation)	Removal efficiency (final)	Photodegradation rate constant (min^{-1})
α-Fe_2O_3	2%	19%	21%	0.0018
α-$AgVO_3$	29%	53%	82%	0.0117
FAV nanocomposite	36%	60%	96%	0.0239

Table 2: Effect of initial MB concentration on the removal efficiency and photodegradation rate constant.

MB Concentration (mg/L)	Removal efficiency (adsorption)	Removal efficiency (photodegradation)	Removal efficiency (final)	Photodegradation rate constant (min^{-1})
10	61%	33%	94%	0.0153
20	36%	60%	96%	0.0239
30	24%	66%	90%	0.0171
40	22%	60%	82%	0.0120

Table 3: Effect of FAV nanocomposite dosage on the removal efficiency and photodegradation rate constant.

FAV nanocomposite Dosage (g/L)	Removal efficiency (adsorption)	Removal efficiency (photodegradation)	Removal efficiency (final)	Photodegradation rate constant (min^{-1})
0.5	24%	67%	91%	0.0186
1.0	36%	60%	96%	0.0239
1.5	59%	39%	98%	0.0312
2.0	57%	39%	96%	0.0211

Table 4: The photocatalytic performance of FAV nanocomposite in comparison with other α-Fe_2O_3 based photocatalysts.

Photocatalyst	Synthesis method	Photocatalytic application	Photocatalytic performance	References
WO_3-Fe_2O_3-rGO (WFG)	Hydrothermal	Removal of RhB and MB	~94% and ~98%	[47]
Fe_2O_3/TiO_2	Sol-gel	Degradation of MB	97%	[48]
CQDs/TiO_2/Fe_2O_3 (CTF)	Multi-step hydrothermal	Degradation of MB	86.5%	[49]
Fe_2O_3/GO/WO_3	Ex-situ and ultrasonic	Degradation of MB, crystal violet (CV) dyes and phenol	98%	[50]
α-Fe_2O_3/α-$AgVO_3$ (FAV)	Hydrothermal and co-precipitation	Removal of MB	98%	This study

removal efficiency of 98% was obtained. According to the data presented in Tables 1-3, the FAV nanocomposite has a relatively high sorption capacity that is desirable for photocatalytic performance. The BET surface area of α-Fe_2O_3 using N_2 adsorption-desorption analysis was 41.859 m^2/g. Thus, the significant sorption capacity of the FAV nanocomposite can be attributed to the relatively high surface area of α-Fe_2O_3, as well as the gel state of α-$AgVO_3$ [40]. Furthermore, the formation of p-n heterojunction between α-Fe_2O_3 and α-$AgVO_3$ enhances the separation of the photogenerated electrons and holes, which decreases the charge carrier recombination rate, and increases the number of oxidizing agents [45]. As a result, the enhanced photocatalytic degradation rate of methylene blue can be due to the synergistic effect of high sorption capacity and heterojunction formation in the FAV nanocomposite.

The photocatalytic efficiency of FAV nanocomposite is compared to that of other α-Fe_2O_3 based photocatalysts from the literature in Table 4 [46]. When compared to other photocatalysts, the photocatalytic performance of the FAV nanocomposite is satisfactory.

Stability of FAV nanocomposite

The stability of FAV nanocomposite was also investigated. After the first run, the nanocomposite was recycled by washing it several times with ethanol

and distilled water, centrifugation, and drying at 80 °C. The photocatalytic reaction was performed by the recycled FAV nanocomposite with a dosage of 1.0 g/L and MB concentration of 20 mg/L. The removal efficiency was 96% after 120 min irradiation which was the same as the removal efficiency in the first run. This result confirms the stability and reusability of the as-synthesized α-Fe_2O_3/α-$AgVO_3$ nanocomposite. Moreover, the simple synthesis technique, easy separation of the photocatalyst, and low energy consumption by the light source are the main advantages for practical applications of the FAV nanocomposite.

Charge transfer mechanism

Fig. 10 schematically shows a possible mechanism for photodegradation of MB over FAV nanocomposite. During UV illumination, electrons of the Valence Band (VB) are transferred to the Conduction Band (CB) due to the photoexcitation of electrons. In the p-n heterojunction formed between α-$AgVO_3$ and α-Fe_2O_3, photoelectrons of the CB of α-$AgVO_3$ can be transferred to the CB of α-Fe_2O_3 because the CB of α-Fe_2O_3 is lower than that of α-$AgVO_3$. Furthermore, the photogenerated holes can be easily transferred from the VB of α-Fe_2O_3 to the VB of α-$AgVO_3$. Therefore, the separation of electrons and holes suppresses the recombination rate, increases the number of hydroxyl radicals, and enhances the degradation rate of MB [39].

CONCLUSIONS

The α-Fe_2O_3/α-$AgVO_3$ nanocomposite was synthesized for photocatalytic applications. A facile solvothermal treatment followed by a co-precipitation method was used to synthesize the nanocomposite. The XRD, FESEM, EDX, FT-IR, and DRS were used to characterize the products. The results revealed that in the FAV nanocomposite, the α-$AgVO_3$ microrods are attached to the nanostructured α-Fe_2O_3 microspheres to form a heterostructure. A slurry annular photoreactor was assembled for photocatalytic experiments. The photocatalytic performance of α-Fe_2O_3/α-$AgVO_3$ nanocomposite was evaluated for MB removal under UV light illumination.

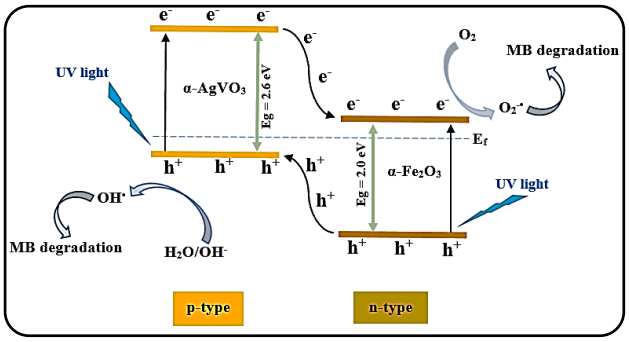

Fig. 10: The charge transfer mechanism for photodegradation of MB over FAV nanocomposite.

The α-Fe_2O_3/α-$AgVO_3$ nanocomposite showed a remarkable efficiency for the removal of MB, which was higher than that of the pure α-Fe_2O_3 and pure α-$AgVO_3$. The effect of pH, MB concentration, and photocatalyst dosage on MB removal was investigated. The optimal conditions were determined as the pH of 5.9, MB concentration of 20 mg/L, and nanocomposite dosage of 1.5 g/L. It was found that the photodegradation reaction follows pseudo-first-order kinetics. Under the optimal conditions, the MB removal efficiency and rate constant were 98% and 0.0312 min^{-1}, respectively. The main benefits for photocatalytic application of the nanocomposite are the stability, simple preparation, easy separation, and low energy consumption by the light source. As a result, the α-Fe_2O_3/α-$AgVO_3$ nanocomposite with improved photocatalytic activity can be used for removing pollutants from aqueous solutions.

Acknowledgments

The authors are grateful to the Azmoon Gostar Sabz Company for kindly collaboration on this study.

Received: Apr. 20, 2022 ; Accepted: Jul. 25, 2022

REFERENCES

[1] Arasteh Nodeh A., Saghi M., Khazaei Nejad M., Preparation, Characterization, and Application of Nanospherical α-Fe_2O_3 Supported on Silica for Photocatalytic Degradation of Methylene Blue, *Iran. J. Chem. Chem. Eng. (IJCCE)*, **38(2):** 21-28 (2019).

[2] Abdullah N., Ayodele B.V., Wan Mansor W.N., Abdullah S., Effect of Incorporating TiO_2 Photocatalyst in PVDF Hollow Fibre Membrane for Photo-Assisted Degradation of Methylene Blue, *Bull. Chem. React. Eng. Catal.*, **13(3):** 588 (2018).

[3] Dehghan Abkenar S., Ganjali M.R., Hossieni M., Sadeghpour Karimi M., Application of Copper Vanadate Nanoparticles for Removal of Methylene Blue from Aqueous Solution: Kinetics, Equilibrium, and Thermodynamic Studies, *Iran. J. Chem. Chem. Eng. (IJCCE)*, **38(6):** 83-92 (2019).

[4] Myneni V.R., Kanidarapu N.R., Vangalapati M., Methylene Blue Adsorption by Magnesium Oxide Nanoparticles Immobilized with Chitosan (CS-MgONP): Response Surface Methodology, Isotherm, Kinetics and Thermodynamic Studies, *Iran. J. Chem. Chem. Eng. (IJCCE)*, **39(6):** 29-42 (2020).

[5] Azimi S.C., Shirini F., Pendashteh A.R., Advanced Oxidation Process as a Green Technology for Dyes Removal from Wastewater: A Review, *Iran. J. Chem. Chem. Eng. (IJCCE)*, **40(5):** 1467-1489 (2021).

[6] Pavithra K.G., P S.K., V J., P S.R., Removal of Colorants from Wastewater: A Review on Sources and Treatment Strategies, *J. Ind. Eng. Chem.*, **75:** 1-19 (2019).

[7] Piramoon S., Aberoomand Azar P., Saber Tehrani M., Mohamadi Azar S., Optimization of Solar-Photocatalytic Degradation of Polychlorinated Biphenyls Using Photocatalyst (Nd/Pd/TiO_2) by Taguchi Technique and Detection by Solid Phase Nano Extraction, *Iran. J. Chem. Chem. Eng. (IJCCE)*, **40(5):** 1541-1553 (2021).

[8] Sharma S., Kumar K., Thakur N., Chauhan S., Chauhan M.S., Eco-friendly Ocimum Tenuiflorum Green Route Synthesis of CuO Nanoparticles: Characterizations on Photocatalytic and Antibacterial Activities, *J. Environ. Chem. Eng.*, **9(4):** 105395 (2021).

[9] Akhtar J., Tahir M.B., Sagir M., Bamufleh H.S., Improved Photocatalytic Performance of Gd and Nd Co-doped ZnO Nanorods for the Degradation of Methylene Blue, *Ceram. Int.*, **46(8):** 11955-11961 (2020).

[10] Fouda A., Hassan S.E.-D., Saied E., Hamza M.F., Photocatalytic Degradation of Real Textile and Tannery Effluent Using Biosynthesized Magnesium Oxide Nanoparticles (MgO-NPs), Heavy Metal Adsorption, Phytotoxicity, and Antimicrobial Activity, *J. Environ. Chem. Eng.*, **9(4):** 105346 (2021).

[11] Mendiola-Alvarez S.Y., Araña J., Doña Rodríguez J.M., Hernández-Ramírez A., Turnes Palomino G., Palomino Cabello C., Hinojosa-Reyes L., Comparison of Photocatalytic Activity of α-Fe_2O_3-TiO_2/P on the Removal of Pollutants on Liquid and Gaseous Phase, *J. Environ. Chem. Eng.*, **9(1):** 104828 (2021).

[12] Yayapao O., Thongtem T., Phuruangrat A., Thongtem S., Ultrasonic-assisted Synthesis of Nd-doped ZnO for Photocatalysis, *Mater. Lett.*, **90**: 83-86 (2013).

[13] Ren Z., Guo Y., Liu C.-H., Gao P.-X., Hierarchically Nanostructured Materials for Sustainable Environmental Applications, *Front. Chem.*, **1:** 18 (2013).

[14] Zhu Y., Peng C., Gao Z.-F., Yang H., Liu W.-M., Wu Z.-J., Hydrothermal Synthesis of $CaFe_2O_4$/α-Fe_2O_3 Composite as Photocatalyst and Its Photocatalytic Activity, *J. Environ. Chem. Eng.*, **6(2):** 3358-3365 (2018).

[15] Mishra M., Chun D.-M., α-Fe_2O_3 as a Photocatalytic Material: A Review, *Appl. Catal., A*, **498:** 126-141 (2015).

[16] Khalil M., Yu J., Liu N., Lee R.L., Hydrothermal Synthesis, Characterization, and Growth Mechanism of Hematite Nanoparticles, *J. Nanopart. Res.*, **16(4):** 1-10 (2014).

[17] Ayachi A.A., Mechakra H., Silvan M.M., Boudjaadar S., Achour S., Monodisperse α-Fe_2O_3 Nanoplatelets: Synthesis and Characterization, *Ceram. Int.*, **41:** 2228-2233 (2015).

[18] Katsuki H., Choi E.-K., Lee W.-J., Hwang K.-T., Cho W.-S., Huang W., Komarneni S., Ultrafast Microwave-hydrothermal Synthesis of Hexagonal Plates of Hematite, *Mater. Chem. Phys.*, **205:** 210-216 (2018).

[19] Wang X., Ammonium Mediated Hydrothermal Synthesis of Nanostructured Hematite (α-Fe_2O_3) Particles, *Mater. Res. Bull.*, **47:** 2513-2517 (2012).

[20] Cao C.Y., Qu J., Yan W.S., Zhu J.F., Wu Z.Y., Song W.G., Low-cost Synthesis of Flowerlike Alpha-Fe_2O_3 Nanostructures for Heavy Metal Ion Removal: Adsorption Property and Mechanism, *Langmuir*, **28(9):** 4573-4579 (2012).

[21] Liang J., Li L., Kang H., Solvothermal Synthesis, Growth Mechanism, and Magnetic Property of Self-assembled 3D Multileaf α-Fe_2O_3 Superstructures, *Powder Technol.*, **235:** 475-478 (2013).

[22] Li S., Hu S., Xu K., Jiang W., Hu J., Liu J., Excellent Visible-Light Photocatalytic Activity of p-type Ag_2O Coated n-type Fe_2O_3 Microspheres, *Mater. Lett.*, **188:** 368-371 (2017).

[23] Noruozi A., Nezamzadeh-Ejhieh A., Preparation, Characterization, and Investigation of the Catalytic Property of α-Fe_2O_3-ZnO Nanoparticles in the Photodegradation and Mineralization of Methylene Blue, *Chem. Phys. Lett.*, **752:** 137587 (2020).

[24] de Melo Monteiro A.P., Dias Holtz R., Carneiro Fonseca L., Zanini Martins C.H., de Sousa M., de Luna L.A.V., de Sousa Maia D.L., Alves O.L., Nano Silver Vanadate $AgVO_3$: Synthesis, New Functionalities and Applications, *The Chemical Record*, **18(7-8):** 973-985 (2018).

[25] Vu T.A., Dao C.D., Hoang T.T.T., Dang P.T., Tran H.T.K., Nguyen K.T., Le G.H., Nguyen T.V., Lee G.D., Synthesis of Novel Silver Vanadates with High Photocatalytic and Antibacterial Activities, *Mater. Lett.*, **123:** 176-180 (2014).

[26] Klockner W., Yadav R.M., Yao J., Lei S., Aliyan A., Wu J., Martí A.A., Vajtai R., Ajayan P.M., Denardin J.C., Serafini D., Melo F., Singh D.P., Acetonitrile Mediated Facile Synthesis and Self-assembly of Silver Vanadate Nanowires into 3D Spongy-like Structure as a Cathode Material for Lithium Ion Battery, *J. Nanopart. Res.*, **19(8):** 288 (2017).

[27] Dong L., Guan G., Wei X., Zhao X., Xv M., Creating SERS Hot Spots on Length Adjustable $AgVO_3$ Nanobelts, *J. Alloys Compd.*, **677:** 12-17 (2016).

[28] Zeng H., Wang Q., Rao Y., Ultrafine β-$AgVO_3$ Nanoribbons Derived from α-$AgVO_3$ Nanorods by Water Evaporation Method and Its Application for Lithium Ion Batteries, *RSC Adv.*, **5(4):** 3011-3015 (2015).

[29] Shariatzadeh S.M.R., Salimi M., Fathinejad H., Hassani Joshaghani A., Nanostructured α-Fe_2O_3: Solvothermal Synthesis, Characterization, and Effect of Synthesis Parameters on Structural Properties, *Int. J. Eng.*, **35(6):** 1186-1192 (2022).

[30] de Oliveira R.C., de Foggi C.C., Teixeira M.M., da Silva M.D.P., Assis M., Francisco E.M., Pimentel B.N.A.d.S., Pereira P.F.d.S., Vergani C.E., Machado A.L., Andres J., Gracia L., Longo E., Mechanism of Antibacterial Activity *via* Morphology Change of α-$AgVO_3$: Theoretical and Experimental Insights, *ACS Appl. Mater. Interfaces*, **9(13):** 11472-11481 (2017).

[31] Yu L., Wang Q., Zhang Z., He J., Guo L., Dong K., Zhang Y., One Pot Synthesize alpha-Fe_2O_3/Graphene Composites and Their Photocatalytic Properties, *Journal of nanoscience and nanotechnology*, **17(2):** 1350-1355 (2017).

[32] Rehman A., Zulfiqar S., Shakir I., Aly Aboud M.F., Shahid M., Warsi M.F., Nanocrystalline Hematite α-Fe_2O_3 Synthesis with Different Precursors and Their Composites with Graphene Oxide, *Ceram. Int.*, **46(6):** 8227-8237 (2020).

[33] McNulty D., Ramasse Q., O'Dwyer C., The Structural Conversion from α-$AgVO_3$ to β-$AgVO_3$: Ag Nanoparticle Decorated Nanowires with Application as Cathode Materials for Li-Ion Batteries, *Nanoscale*, **8(36):** 16266-16275 (2016).

[34] Tadic M., Trpkov D., Kopanja L., Vojnovic S., Panjan M., Hydrothermal Synthesis of Hematite (α-Fe_2O_3) Nanoparticle Forms: Synthesis Conditions, Structure, Particle Shape Analysis, Cytotoxicity and Magnetic Properties, *J. Alloys Compd.*, **792:** 599-609 (2019).

[35] Trpkov D., Panjan M., Kopanja L., Tadić M., Hydrothermal Synthesis, Morphology, Magnetic Properties and Self-assembly of Hierarchical α-Fe_2O_3 (Hematite) Mushroom-, Cube- and Sphere-like Superstructures, *Appl. Surf. Sci.*, **457:** 427-438 (2018).

[36] Tadic M., Lazovic J., Panjan M., Kralj S., Hierarchical Iron Oxide Nanocomposite: Bundle-like Morphology, Magnetic Properties and Potential Biomedical Application, *Ceram. Int.*, **48(11):** 16015-16022 (2022).

[37] Zheng X., Huang M., You Y., Peng H., Wen J., Core-shell Structured α-Fe_2O_3@CeO_2 Heterojunction for the Enhanced Visible-Light Photocatalytic Activity, *Mater. Res. Bull.*, **101:** 20-28 (2018).

[38] Soares da Silva J., Machado T.R., Martins T.A., Assis M., Foggi C.C., Macedo N.G., Beltran-Mir H., Cordoncillo E., Andres J., Longo E., Alpha-$AgVO_3$ Decorated by Hydroxyapatite ($Ca_{10}(PO_4)_6(OH)_2$): Tuning Its Photoluminescence Emissions and Bactericidal Activity, *Inorg. Chem.*, **58(9):** 5900-5913 (2019).

[39] Wang H., Zhang L., Chen Z., Hu J., Li S., Wang Z., Liu J., Wang X., Semiconductor Heterojunction Photocatalysts: Design, Construction, and Photocatalytic Performances, *Chem. Soc. Rev.*, **43(15):** 5234 (2014).

[40] Mondal C., Ganguly M., Pal J., Sahoo R., Sinha A.K., Pal T., Pure Inorganic Gel: A New Host with Tremendous Sorption Capability, *Chem Commun (Camb)*, **49(82):** 9428-9430 (2013).

[41] Imran M., Abutaleb A., Ashraf Ali M., Ahamad T., Rahman Ansari A., Shariq M., Lolla D., Khan A., UV Light Enabled Photocatalytic Activity of α-Fe_2O_3 Nanoparticles Synthesized *via* Phase Transformation, *Mater. Lett.*, **258:** 126748 (2020).

[42] Shokri A., Mahanpoor K., Soodbar D., Evaluation of A Modified TiO_2 (GO–B–TiO_2) Photo Catalyst for Degradation of 4-Nitrophenol in Petrochemical Wastewater by Response Surface Methodology Based on the Central Composite Design, *J. Environ. Chem. Eng.*, **4(1):** 585-598 (2016).

[43] Vu X.H., Phuoc L.H., Dien N.D., Pham T.T.H., Thanh L.D., Photocatalytic Degradation of Methylene Blue (MB) over α-Fe_2O_3 Nanospindles Prepared by a Hydrothermal Route, *J. Electron. Mater.*, **48(5):** 2978-2985 (2019).

[44] Sivaranjani R., Thayumanavan A., Sriram S., Photocatalytic Activity of Zn-doped Fe_2O_3 Nanoparticles: A Combined Experimental and Theoretical Study, *Bull. Mater. Sci.*, **42(4):** 185 (2019).

[45] Zhang J., Wang J., Xu H., Lv X., Zeng Y., Duan J., Hou B., The Effective Photocatalysis and Antibacterial Properties of AgBr/$AgVO_3$ Composites under Visible-light, *RSC Adv.*, **9(63):** 37109-37118 (2019).

[46] Hitam C.N.C., Jalil A.A., A Review on Exploration of Fe_2O_3 Photocatalyst Towards Degradation of Dyes and Organic Contaminants, *J. En. Man.*, **258:** 110050 (2020).

[47] Priyadharsan A., Vasanthakumar V., Shanavas S., Karthikeyan S., Anbarasan P.M., Crumpled Sheet like Graphene Based WO_3-Fe_2O_3 Nanocomposites for Enhanced Charge Transfer and Solar Photocatalysts for Environmental Remediation, *Appl. Surf. Sci.*, **470:** 114-128 (2019).

[48] Ahmed M.A., El-Katori E.E., Gharni Z.H., Photocatalytic Degradation of Methylene Blue Dye Using Fe_2O_3/TiO_2 Nanoparticles Prepared by Sol–gel Method, *J. Alloys Compd.*, **553:** 19-29 (2013).

[49] Zhang J., Kuang M., Wang J., Liu R., Xie S., Ji Z., Fabrication of Carbon Quantum Dots/TiO_2/Fe_2O_3 Composites and Enhancement of Photocatalytic Activity under Visible Light, *Chem. Phys. Lett.*, **730:** 391-398 (2019).

[50] Mohamed H.H., Rationally Designed Fe_2O_3/GO/WO_3 Z-Scheme Photocatalyst for Enhanced Solar Light Photocatalytic Water Remediation, *J. Photochem. Photobiol. A: Chem.*, **378:** 74-84 (2019).